Chemical Engineering Science 299 (2024) 120557

Contents lists available at ScienceDirect

Chemical Engineering Science

journal homepage: www.elsevier.com/locate/ces

Shapes and terminal velocities of single bubbles rising through fiber bundle in stagnant water

Ryo Kurimoto [a,*], Roberta Fátima Neumeister [b], Ryuya Komine [a], Gherhardt Ribatski [b], Kosuke Hayashi [a]

[a] Graduate School of Engineering, Kobe University, 1-1, Rokkodai, Nada, Kobe, Japan
[b] Heat Transfer Research Group, São Carlos School of Engineering, University of São Paulo, São Carlos, Brazil

ARTICLE INFO

Keywords:
Bubble
Shape
Terminal velocity
Fiber bundle
Drag coefficient

ABSTRACT

The shapes and terminal velocities of single bubbles in the surface tension force and the inertial force dominant regime were measured in a vertical bundle consisting of fluorinated ethylene propylene fibers of 2 mm diameter. Three kinds of fiber arrangements were tested with the fiber pitches L_p of 18, 12, and 6 mm. The terminal velocities in the bundles were larger than those in the absence of a fiber bundle and increased with decreasing L_p. The bubble shapes were significantly deformed by fibers, which would be the cause of the velocity increase, i.e., a reduction in the form drag. The terminal velocities in the bundles were well predicted by the combination of the drag correlation in the absence of a fiber bundle and the multiplier for bubbles in fiber bundles.

1. Introduction

Filtration with membranes is used in various water purification systems, e.g., hollow fiber membranes are utilized in membrane bioreactors (MBRs) to obtain purified water by separating particulate contaminants from wastewater (Akhondi et al., 2017). In MBRs, aeration plays a role not only in oxygen supply to microbes but also in prevention and removal of deposition of contaminants on membrane surfaces (Wang et al., 2014; Wibisono et al., 2014; Kurimoto et al., 2021). Energy consumption in aeration, however, is large and is a significant portion of MBR systems (Böhm et al., 2012; Tang, et al., 2022). It is therefore important to understand the characteristics of bubbly flows inside and around a bundle of hollow fiber membranes for the design and development of effective aeration systems. It has been reported that the bubble size distribution in a bundle of hollow fiber membranes is usually broad due to frequent breakup and coalescence of bubbles, resulting in the formation of bubbles of various shapes from ellipsoids to caps (Inoue et al., 2016; Radaei et al., 2019; Kurimoto et al., 2023). The structure of bubbly flows in MBRs is determined as a consequence of interaction between the bioreactor-scale flow motion and the motion of bubbles. Detailed knowledge on the motion of bubbles rising through a fiber bundle, therefore, is of great importance to understand the dynamics of bubbly flows in MBRs.

In contrast to the study on single bubbles in infinite stagnant liquid, there are only a few studies on single bubbles in a fiber bundle in literature. However, there are studies on the shapes and terminal velocities of single bubbles in a fuel rod bundle in nuclear reactors and a tube bundle for heat exchangers in chemical reactors. Venkateswararao et al. (1982) measured the terminal velocities of single bubbles rising through a rod bundle consisting of 12.7 mm vertical rods in an 88.9 mm circular column. The terminal velocities increased with increasing the bubble diameter d for $4 < d < 8$ mm and became larger than those in infinite liquids for $d \geq 5$ mm. Cell-Taylor bubbles, whose horizontal cross section occupied a subchannel enclosed by four rods, were independent of d. Shroud Taylor bubbles, the sizes of which were larger than that of the subchannel, took terminal velocities larger than the theoretical velocity of Taylor bubbles (Dumitrescu, 1943). Tomiyama et al. (2003) measured the terminal velocities of single bubbles rising through the inner subchannel enclosed by a 2 x 2 rod bundle in a square duct. The width of the duct was 27.2 mm, and the diameter of the rods was 12.0 mm. They classified terminal velocity data into three regimes based on the bubble shapes: the spheroidal, cap and cell-Taylor regimes. The terminal velocities of spheroidal bubbles decreased with increasing d, while those of cap bubbles increased with increasing d. In the cell-Taylor regime, the terminal velocities asymptotically approached the constant value reported by Venkateswararao et al. (1982). They also reported that the terminal velocities of spheroidal and cap bubbles agree with a model based on a potential-flow approximation in the vicinity of the

* Corresponding author.
E-mail address: kurimoto@mech.kobe-u.ac.jp (R. Kurimoto).

https://doi.org/10.1016/j.ces.2024.120557
Received 14 May 2024; Received in revised form 9 July 2024; Accepted 23 July 2024
Available online 24 July 2024

bubble nose (Tomiyama et al., 2002), and an empirical velocity correlation was developed for cell-Taylor bubbles. Cioncolini and Magnini (2021) observed the motion of single bubbles for $3 \leq d \leq 6$ mm rising near a rod of 9.99 mm diameter in a square duct of 25.3 mm width. They showed that the measured aspect ratios and terminal velocities were comparable to those measured in Tomiyama et al. (2003).

Concerning a report on the effects of vertical thin rods on bubble motion, Zhou and Prosperetti (2021) considered the terminal velocity of a Taylor bubble rising through a cylindrical cage of thin vertical rods set in a pipe. The ratio of the rod diameter to the pipe diameter was less than 0.067. The presence of the rods surrounding a Taylor bubble increased the amount of liquid downflow within the liquid film formed between the rods and the bubble, resulting in the terminal velocities of the bubble with the cylindrical cage being at most 1.7 times larger than that without the cage. The bubbles took on pleated interfaces on those sides due to the presence of the rods, which implies that bubbles rising through a fiber bundle can take on complex shapes.

To the authors' best knowledge, there have been no studies on the shapes and terminal velocities of single bubbles rising through a bundle consisting of fibers, i.e., rods with the order of a few millimeters in diameter, in a square arrangement. Single bubbles rising through 2-mm fibers in stagnant water were therefore dealt with in the present study; the shapes, the terminal velocities, and the horizontal motion of the bubbles were analyzed for three fiber arrangements with different fiber pitches between fibers. A drag coefficient correlation for bubbles rising through fiber bundles was developed and its applicable range covers from 4.2 (ellipsoidal) to 18.7 mm (cap/shroud-Taylor).

2. Experimental method

Fig. 1 shows the experimental setup consisting of the square tank and a fiber bundle. The tank was made of transparent acrylic resin and its width and height were 160 and 1110 mm, respectively. The tank was filled with the liquid phase up to 1100 mm. Circular fibers of 2 mm diameter were made of fluorinated ethylene propylene (FEP) resin, whose refractive indexes are almost the same as that of water, i.e., the difference is less than 0.5 %. It is therefore possible to obtain bubble images without optical distortion at the fiber surfaces (Tomiyama et al., 2003). The fibers were fixed at the upper and lower plates and the distance between them was 770 mm. They were tightly aligned and the relaxation of the fibers was less than 1 mm at the middle elevation. Experiments were carried out at room temperature (298 ± 0.5 K) and atmospheric pressure.

Fig. 2 shows the cross-sectional views of the fiber arrangements. Fig. 2(a) shows the relation between the sizes of the tank and the fiber bundle. The fiber bundle was set in the center region of the tank. Three fiber arrangements were tested as shown in Fig. 2(b)-(d), i.e., 4 × 4 fiber bundle with $L_p = 18$ mm, 6 × 6 fiber bundle with $L_p = 12$ mm, and 12 × 12 fiber bundle with $L_p = 6$ mm, where L_p is the distance between the centers of adjacent fibers.

Purified water (Merck, Elix Essential UV5) was used as the liquid phase. The surface tension σ was measured by the pendant bubble method (Pan et al., 1998; Mori, et al., 2024). The measured σ was 0.072 N/m and its uncertainty estimated at 95 % confidence in measured σ was 0.65 %. The liquid density ρ_L and the liquid viscosity μ_L given in literature and the measured σ were used in calculations of the dimensionless numbers.

As shown in Fig. 1, a single bubble was released from the horizontal nozzle, which was placed 60 mm above the bottom of the bundle, by using the gas syringe. Images of single bubbles were obtained by using a high-speed video camera (Photron, FASTCAM Mini AX50, frame rate = 1000 frame/s, spatial resolution ≈ 0.087 mm/pixel) at 500 mm above the nozzle. The diameter d of a single bubble was predetermined by the scale of the syringe. The range of d was 4.2–18.7 mm. The uncertainty estimated at 95 % confidence in d was less than 8 % for bubbles with $d \geq$ 5.8 mm and reached 18 % for smaller bubbles. Ten bubbles were measured at each d.

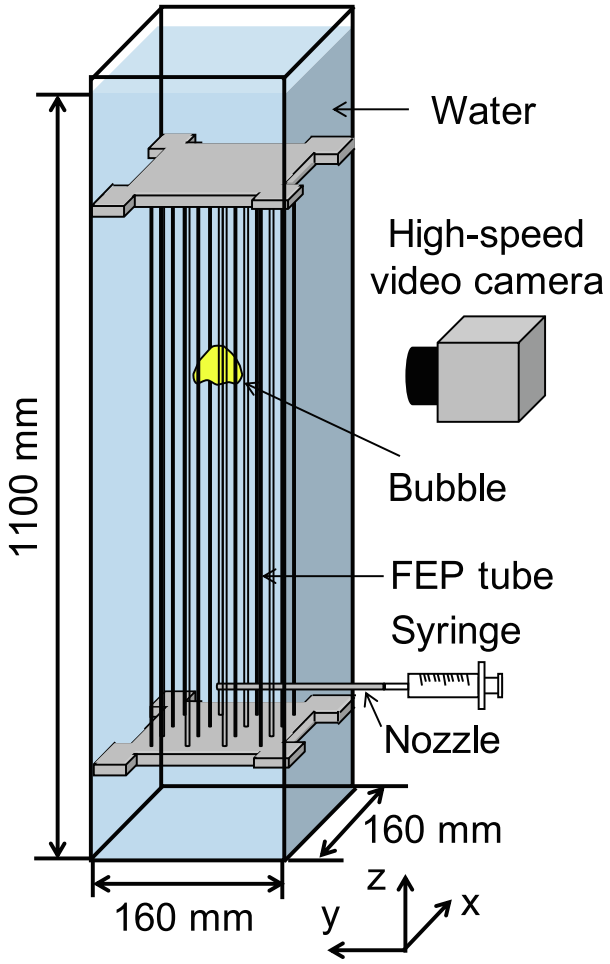

Fig. 1. Experimental setup.

The terminal velocities, V_{T0} in the absence of a fiber bundle and V_T in the presence of the fiber bundle, the bubble aspect ratio E, and the geometric center of the bubble image were calculated by means of image processing, where E is defined by the ratio of the maximum vertical dimension d_v to the maximum horizontal dimension d_h:

$$E = \frac{d_v}{d_h} \tag{1}$$

The d_v and d_h were obtained by fitting ellipsoidal shape to bubbles for $d \leq 5.8$ and rectangular shape to bubbles for $d \geq 7.3$ mm. The time duration for the traveling distance of about 60 mm in the vertical direction was measured to obtain the terminal velocity. The drag coefficients, C_{D0} in the absence of a fiber bundle and C_D in the presence of the fiber bundle, were evaluated by using the relation between the drag and buoyant forces:

$$C_{D0} = \frac{4(\rho_L - \rho_G)gd}{3V_{T0}^2\rho_L} \tag{2}$$

$$C_D = \frac{4(\rho_L - \rho_G)gd}{3V_T^2\rho_L} \tag{3}$$

where ρ_G is the gas density, and g the magnitude of the acceleration of gravity. The drag ratio is therefore $C_D/C_{D0} = V_{T0}^2/V_T^2$. The geometric center $\boldsymbol{G}$ of a bubble was calculated by

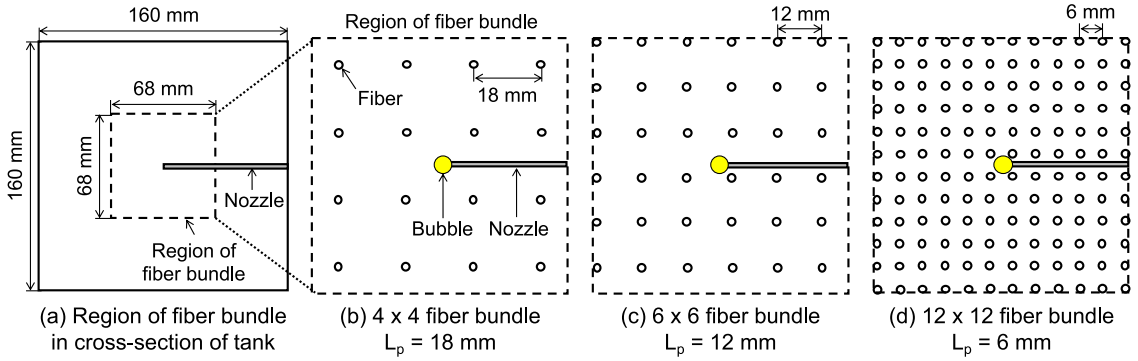

Fig. 2. Arrangement of fibers in the tank cross section.

$$\boldsymbol{G} = \frac{\sum_{i=1}^{m}\sum_{k=1}^{n}\boldsymbol{r}_{i,k}\phi_{i,k}}{\sum_{i=1}^{m}\sum_{k=1}^{n}\phi_{i,k}} \tag{4}$$

where ϕ is the phase indicator ($\phi = 1$ for the gas phase and $\phi = 0$ for the liquid phase), $\boldsymbol{r}$ (= (x, z)) the position vector, the subscripts i and k denote the pixel number in the x and z directions, and x and z are the horizontal and vertical coordinates, respectively. The uncertainties estimated at 95 % confidence in V_T, E, and $\boldsymbol{G}$ were less than 6.5, 11, and 18 %, respectively.

3. Results and discussion

3.1. Experimental results

Fig. 3(a) shows bubble shapes in the absence of a fiber bundle, and Fig. 3(b) shows the trajectories of bubbles in the absence of a fiber bundle, where $x^* = (x–X)/d$ and X is the initial value of x. The bubble at d = 4.2 mm exhibits an ellipsoidal shape and lateral motion with amplitude comparable to its diameter. The bubbles at d = 5.8, 10.5, and 12.4 mm show wobbling motion with lateral motion, whose amplitude decreases with increasing d. Further increase in d makes the bubble of d = 18.7 mm to have a cap-like shape and its trajectory is almost rectilinear. The slight lateral displacement observed is due to oscillation of the bubble shape. Thus, bubbles in the absence of fibers are classified into either the ellipsoidal ($d \leq 5.3$ mm), the wobbling ($5.8 \leq d \leq 13.9$ mm), or the cap bubble regime ($d \geq 15.6$ mm).

Bubbles in the 12 × 12 fiber bundle (L_p = 6 mm) and their trajectories are shown in Fig. 4(a) and 4(b), respectively. Videos of bubble motion are also provided in Supplementary videos 4–6 as listed in Table A1. Although the bubble at d = 4.2 mm is classified into the ellipsoidal regime, its shape is more rounded than that without fibers (Fig. 3(a)). The lateral motion was largely attenuated in some of the ten runs due to confinement effects by fibers as observed for bubbles in a bundle of 12-mm rods (Tomiyama et al., 2003). The bubble at d = 5.8 mm (~L_p) fits the cell enclosed by four fibers and wobbling motion as observed in the absence of a fiber bundle does not appear. The presence of the fibers also largely mitigates the wobbling motion of the bubbles at d = 10.5 and 12.4 mm, resulting in the rectilinear rise paths. The width of the cap bubble (d = 18.7 mm) is thinner than that in the absence of fibers, and an increase in the curvature at the bubble front is observed. The shape oscillation is also much weaker than in Fig. 3(a), which is attributed to damping of capillary waves by the fibers.

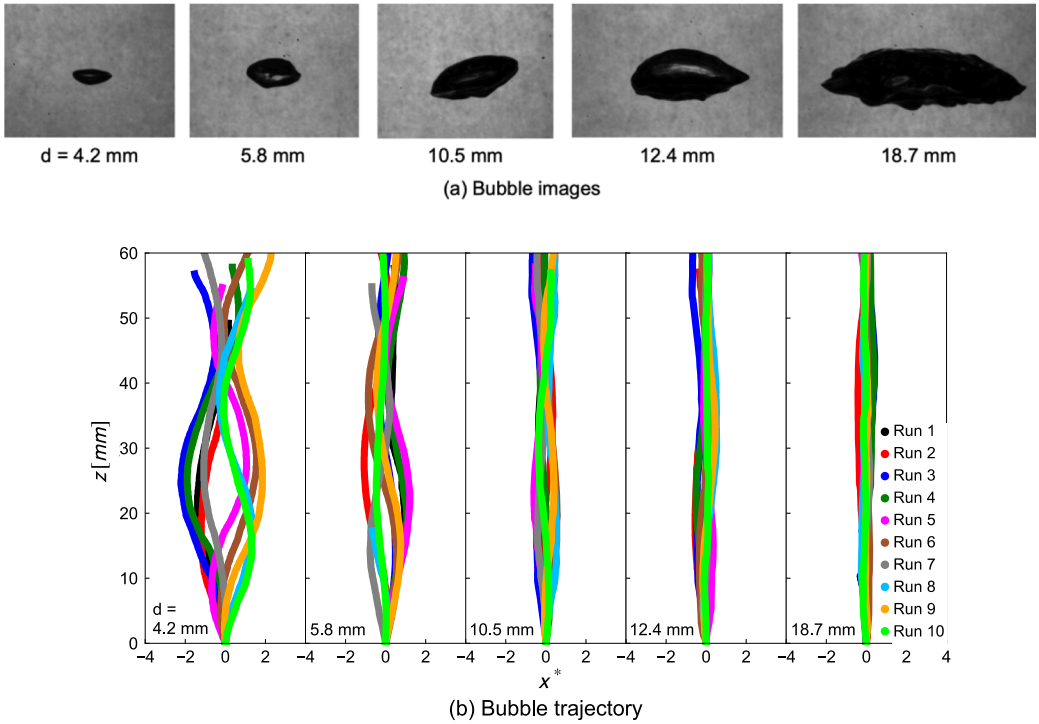

Fig. 3. Bubble shapes and bubble trajectories in the absence of fiber bundle.

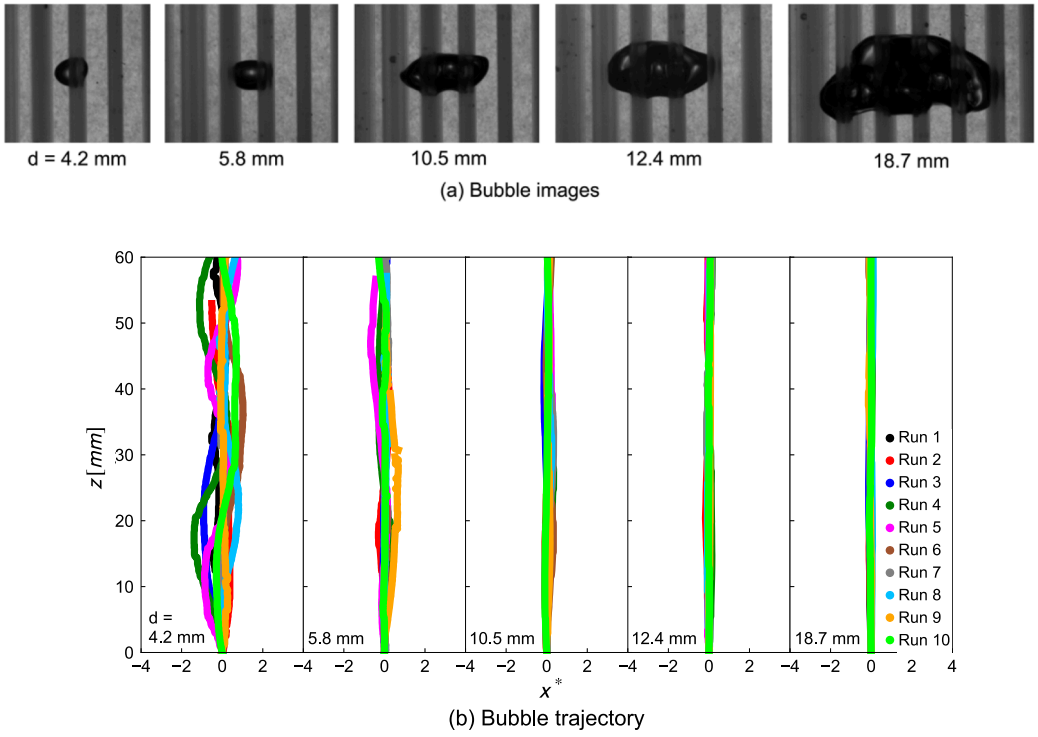

Fig. 4. Bubble shapes and bubble trajectories in 12 × 12 fiber bundle.

We do not present bubble images and trajectories for the 4 × 4 and 6 × 6 fiber bundles in this section to avoid making the paper lengthy; Instead, bubble motion in the 6 × 6 fiber bundle can be found in supplementary videos 1–3 as listed in Table A1 and bubble images in the 4 × 4 and 6 × 6 fiber bundles are exhibited in Figs. B1 and B2.

Fig. 5 shows the terminal velocities of single bubbles. The data are the mean values of the ten runs. See Fig. C1 in Appendix C for the variance of the data. The terminal velocity in the no-fiber case slightly decreases with increasing d up to $d = 7.3$ mm and then increases with increasing d. This trend agrees well with the terminal velocity $V_{T\infty}$ of a single bubble in infinite stagnant liquids calculated by the following correlation of the drag coefficient $C_{D\infty}$ for bubbles in infinite stagnant liquids (Tomiyama et al., 1998) with the force balance $V_{T\infty} = [4(\rho_L - \rho_G)gd/3C_{D\infty}\rho_L]^{1/2}$ as shown by the black line in the figure:

$$C_{D\infty} = max\left\{ min\left[\frac{16}{Re_\infty}\left(1 + 0.15Re_\infty^{0.687}\right), \frac{48}{Re_\infty}\right], \frac{8}{3}\frac{Eo}{Eo+4}\right\} \tag{5}$$

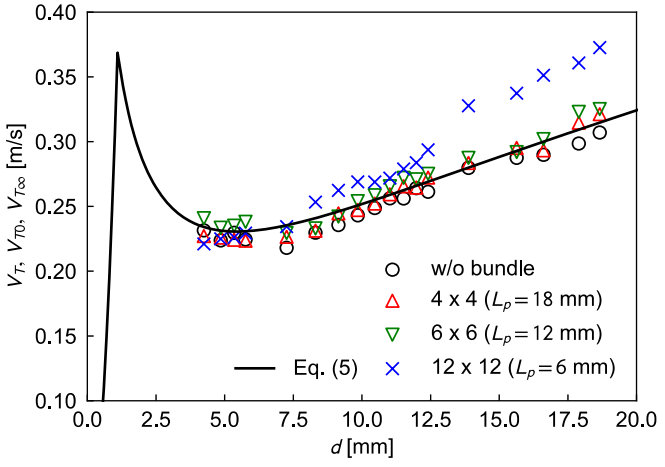

Fig. 5. Terminal velocities of bubbles.

where Re_∞ and Eo are the bubble Reynolds number in infinite stagnant liquids and the Eötvös number, respectively, defined by

$$Re_\infty = \frac{\rho_L V_{T\infty} d}{\mu_L} \tag{6}$$

$$Eo = \frac{(\rho_L - \rho_G)gd^2}{\sigma} \tag{7}$$

The bubble Reynolds number Re_0 in the absence of a fiber bundle and the bubble Reynolds number Re in the fiber bundle are defined by

$$Re_0 = \frac{\rho_L V_{T0} d}{\mu_L} \tag{8}$$

$$Re = \frac{\rho_L V_T d}{\mu_L} \tag{9}$$

The ranges of Re_0, Re, and Eo in the present experiments are $1100 \le Re_0 \le 6420$, $1050 \le Re \le 7800$, and $2.4 \le Eo \le 47$, respectively. All the bubbles are in the Eo-controlling regime of Eq. (5), i.e., the surface tension force and the inertial force are dominant rather than the viscous force. The measured V_T in the 4 × 4 fiber bundle are comparable to V_{T0}, while those in the 6 × 6 bundle are slightly larger. For $4.2 \le d \le 7.3$ mm, the differences in V_T by the fiber arrangement are not remarkable. On the other hand, in the range of $d \ge 8.3$ mm, V_T increases with decreasing L_p and in particular the amount of increase in V_T is remarkable with the 12 × 12 bundle for the cap-bubble regime ($d \ge 13.9$ mm). As can be seen in Fig. 3(a) and 4(a), the change in the bubble shape is also remarkable in the cap-bubble regime. Therefore, the difference in the rate of increase in V_T might relate to the change in the bubble shape. Venkateswararao et al. (1982) and Tomiyama et al. (2003) reported that cell-Taylor bubbles appeared in rod bundles and had a constant terminal velocity, which demonstrates that, being similar to Taylor bubbles in vertical conduits (Hayashi, et al., 2010), the bundle geometry (the hydraulic diameter and the rod pitch) governs the terminal velocity of a cell-Taylor bubble, not the sphere-volume-equivalent bubble diameter. The cell-Taylor regime was not observed in the present experiments. The

confinement ratios of the rod or fiber diameter to the pitch are 0.73 in Venkateswararao et al. (1982), 0.79 in Tomiyama et al. (2003), and 0.33 in the 12 × 12 bundle of the present study. The confinement effect is therefore weak in the present study and bubbles could penetrate into the side subchannels so that cell-Taylor bubbles were not formed.

Experiments on single bubbles rising through a 6 × 6 bundle with L_p = 6 mm, i.e., the same L_p as the 12 × 12 bundle, consisting of stainless steel fibers of 2 mm diameter or FEP fibers of 2 mm diameter were also carried out to understand effects of materials of fibers on V_T, since stainless steel and FEP have hydrophilic and hydrophobic properties, respectively (Li and Neumann, 1992; Lin and Chang, 2011). The averaged V_T of ten bubbles at each d for 12.4 ≤ d ≤ 15.6 mm were comparable to those in the 12 × 12 bundle and varied less than 2.6 % due to the difference in the materials. The surface wettability therefore does not affect significantly V_T in the present fiber bundles.

The mean bubble aspect ratio is plotted against Eo in Fig. 6. The aspect ratio decreases with increasing Eo. The aspect ratios for Eo ≤ 7.1 and Eo ≥ 33 in the 12 × 12 bundle are larger than those under the other conditions, while the effects of L_p on E are small in the 4 × 4 and 6 × 6 bundles. The larger E in the 12 × 12 bundle for Eo ≤ 7.1 is attributed to wall effects by fibers. As shown in Fig. 5, V_T in the 12 × 12 bundle are comparable to the other data for 2.4 ≤ Eo ≤ 4.5 (4.2 ≤ d ≤ 5.8 mm) despite the larger E. This might be because the dependence of V_T on E becomes weak with increasing d (Tomiyama et al., 2002). In the case of cap bubbles in infinite water, the increase in E makes V_T smaller (Tomiyama, 2004). Therefore, the increase in V_T despite the increase in E for Eo ≥ 33 implies that the actual shapes of large bubbles in the presence of fiber bundles would be significantly different from cap shapes.

Top views of a large bubble rising through the fiber bundle were therefore recorded by using the high-speed video camera with a borescope (Olympus, R080) to understand its 3D shape by recording the side views of the bubble simultaneously. The borescope was inserted into the 12 × 12 bundle from the top side of the tank. It should be noted that the 2 × 2 fibers arranged in the center of the 12 × 12 bundle were removed to make room for inserting the borescope. Fig. 7(a-i) and (a-ii) show the side and top views, respectively, of a bubble of d = 18.7 mm at the same instant. The terminal velocities of bubbles with the bundle configuration for the borescope observation agreed with those in the 12 × 12 bundle within a difference of only about 1.0 %, meaning that the removal of the 2 × 2 fibers in the center region did not make a large impact on the dynamics of bubbles. At least four lines of fibers are assigned to the side of the bubble shown in Fig. 7(a-i). The bubble contour is represented by the white dashed line in Fig. 7(a-ii). It can be seen that the bubble has a core region in the central open space without the 2 × 2 fibers and several legs branch at the fibers. However, the lengths of the legs are short since

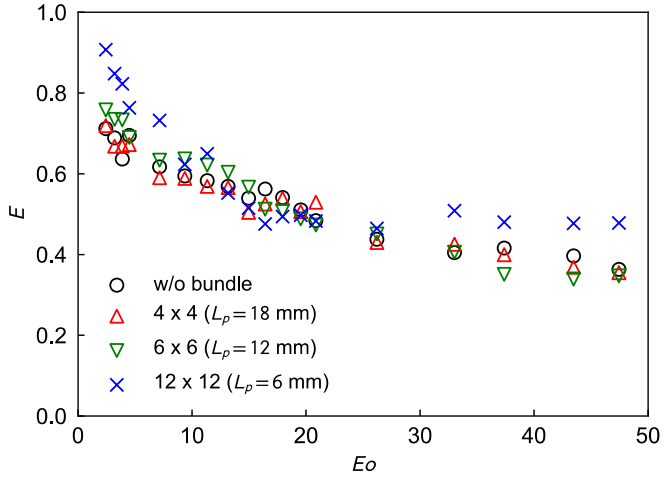

Fig. 6. Bubble aspect ratio E.

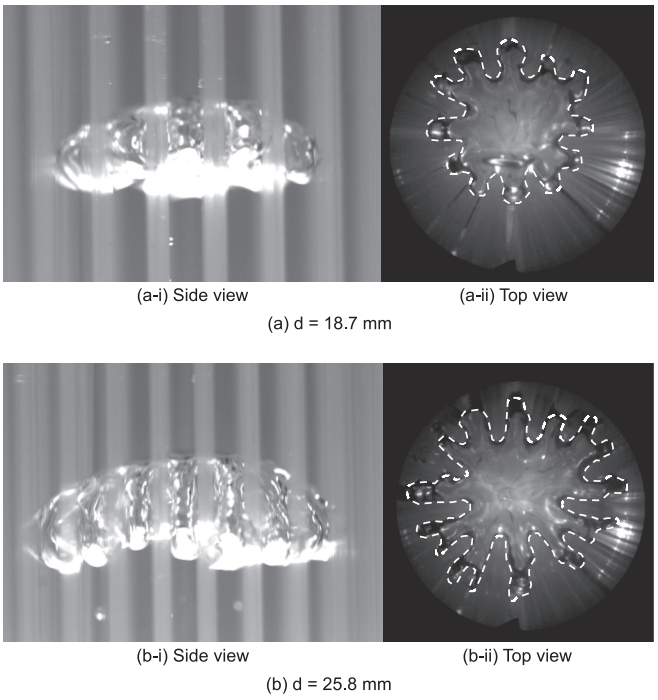

Fig. 7. Side and top views of bubbles rising in 12 × 12 bundle without 2 × 2 fibers in center region.

most part of the bubble exists in the central open space. The volume of the bubble is therefore insufficient to shroud fibers due to the presence of the central open space. Fig. 7(b-i) and (b-ii) (Supplementary video 7) show simultaneous images of the side and top views of a bubble with d = 25.8 mm, respectively, i.e., purposely larger d than the maximum d (=18.7 mm) in the experimental range for the V_T measurement. At least six lines of fibers are assigned to the side of the bubble shown in Fig. 7(b-i). Fig. 7(b-ii) shows that the structure of the bubble, i.e., a core region and several legs, is not so different from the bubble of d = 18.7 mm except for the longer legs. Most of the legs, which extend in each straight line, do not coalesce to each other, so that the bubble does not shroud all fibers in the projected area of the circumscribed circle of the bubble completely, i.e., most of the fibers do not penetrate the bubble. This implies that large bubbles with much larger width than L_p in a fiber bundle might take cross-like shapes and their characteristics would be significantly different from those of cap bubbles in infinite water, which would contribute to the increase in V_T, i.e., a reduction in the form drag, and justify the increase in the aspect ratio observed for d ≥ 15.6 mm (Eo ≥ 33) in Fig. 6.

Fig. 8 shows the standard deviation σ* of the displacement of the bubble center position in the horizontal direction normalized by d. The plotted data represent the averaged values of measured bubbles at each d. The relation between the measured and averaged σ* is shown in Fig. C2 in Appendix C. The standard deviation steeply decreases with increasing Eo for Eo ≤ 4.5. Within the range of 7.1 ≤ Eo ≤ 21, the standard deviations remain nearly constant in the absence of a fiber bundle and the presence of the 4 × 4 and 6 × 6 bundles. The decrease in σ* in the 6 × 6 bundle is more remarkable compared to both the absence of a bundle and the presence of the 4 × 4 bundle, since σ* in the 6 × 6 bundle are larger for 26 ≤ Eo ≤ 38, which might be due to large shape deformation during horizontally passing through the gap of fibers, followed by a decrease for Eo ≥ 43, attributed to restriction imposed by the fibers. In the 12 × 12 bundle, σ* exhibits a jump at Eo = 7.1, followed by a decrease with increasing Eo for 9.4 ≤ Eo ≤ 21, and then stabilizes for Eo ≥ 26. These results therefore indicate strong restriction on the horizontal motion of a single bubble within the 12 × 12 bundle.

The standard deviation is then plotted against the ratio λ_f of d to L_p in

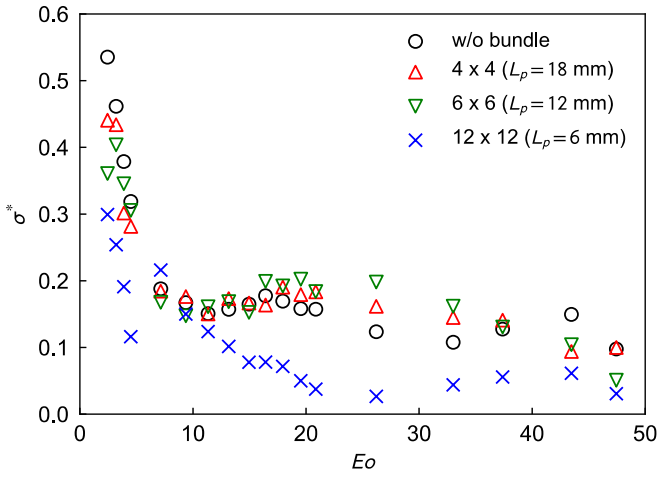

Fig. 8. Standard deviation of displacement of bubble center position.

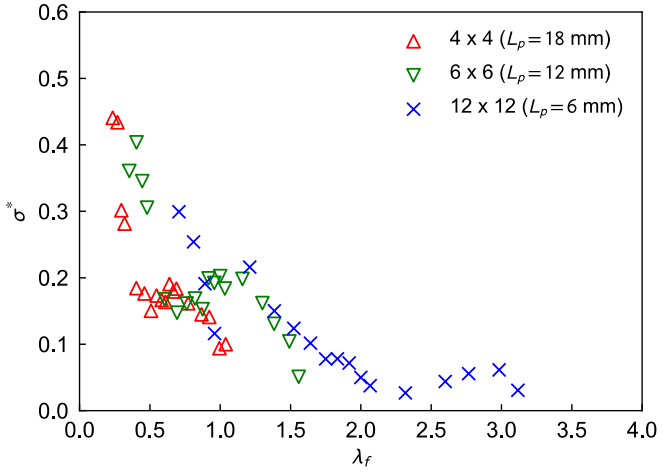

Fig. 9. Relation between σ* and λ_f (=d/L_p).

Fig. 9. Notably, a decrease in σ* at $\lambda_f \approx 1$ is observed, with the 4 × 4 fiber bundle showing this decrease starting at a lower λ_f than unity. As shown in Fig. 8, σ* in the 4 × 4 bundle are comparable to those in the absence of fibers, suggesting weak effects of fibers on σ* in this configuration. The jump in σ* in the 12 × 12 bundle occurs at $\lambda_f \approx 1.2$. The bubble at $\lambda_f =$ 0.95, i.e., $Eo = 4.5$ ($d = 5.8$ mm), fits within the cell enclosed by four fibers as shown in Fig. 4(a), restricting horizontal motion. At $\lambda_f = 1.2$, i.e., $Eo = 7.1$ ($d = 7.3$ mm), a part of a bubble bulges out from the cell, making the restriction by fibers weak due to the presence of a space between the bubble and fibers in the neighbor cell, facilitating some horizontal motion recovery. Decreases in σ* begin at $\lambda_f \approx 1.3$ in both 6 × 6 and 12 × 12 bundles, indicating restriction by the outer fibers around the cell enclosed by four fibers. The nearly constant standard deviation observed for the 4 × 4 and 6 × 6 fiber bundles in Fig. 8 is identified in Fig. 9 between $0.5 \leq \lambda_f \leq 1.3$, reinforcing the influence of the fiber pitch distance. The λ_f might therefore be one of the clues to understand the motion of bubbles rising through not only fiber bundles but also rod and tube bundles.

3.2. C_D correlation

Fig. 10 shows the drag coefficients. The dashed line is Eq. (5) for the *Eo*-controlling regime. The solid line is the drag coefficient C_{D0} calculated by combining $C_{D\infty}$ and the wall effect multiplier ϕ_w to account for the presence of the tank wall, i.e.,

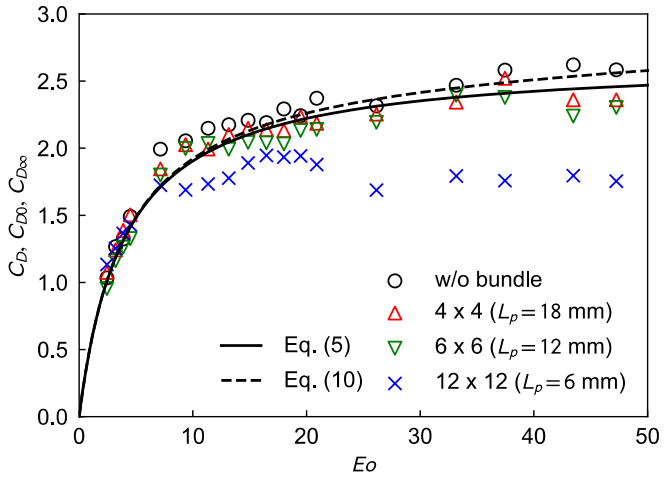

Fig. 10. Drag coefficients of bubbles.

$$C_{D0} = C_{D\infty}\phi_w \tag{10}$$

where the following ϕ_w correlation for bubbles and drops through a vertical pipe in the surface tension force and the inertial force dominant regime (Clift et al., 1978; Kurimoto et al., 2013) was used:

$$\phi_w = \left(1 - \lambda^2\right)^{-3} \tag{11}$$

where λ is the ratio of d to the width of the tank. Equation (10) agrees with the data of the no fiber case rather than Eq. (5), which means that large bubbles were under the influence of the tank wall. For $Eo \leq 4.5$, the measured data lie on the correlations. For $Eo \geq 7.1$, C_D tends to decrease with decreasing L_p as expected from the velocity data.

By adopting a multiplier ϕ_f for the effects of fiber bundles, let us express C_D for $Eo \geq 7.1$ as

$$C_D = C_{D0}\left(1 + \phi_f\right) \tag{12}$$

Solving this equation for ϕ_f gives

$$\phi_f = \frac{C_D}{C_{D0}} - 1 \tag{13}$$

Thus, ϕ_f can be calculated by substituting the measured C_D and C_{D0}. The relation between ϕ_f and *Eo* for $Eo \geq 7.1$ is shown in Fig. 11. The ϕ_f in the 4 × 4 bundle are close to zero, while those in the 6 × 6 bundle are slightly lower than zero. In the 12 × 12 bundle, ϕ_f are lower than those in the 6 × 6 bundle. The decrease in ϕ_f due to the increase in *Eo* becomes remarkable with decreasing L_p.

The ϕ_f for $Eo \geq 7.1$ are shown against λ_f in Fig. 12. The ϕ_f decreases with increasing λ_f and is well correlated in terms of λ_f. The λ_f is therefore a primal indicator for the fiber effects on the drag coefficient in addition to the horizontal motion shown in Fig. 9. The relation between ϕ_f and λ_f is expressed as

$$\phi_f = -0.0773\lambda_f^{1.29} \tag{14}$$

Based on the above discussion, the C_D data can be expressed as

$$C_D = C_{D\infty}\phi_w\left(1 + \phi_f\right) \tag{15}$$

The drag ratio is expressed as $C_D/C_{D\infty} = V_{T\infty}^2/V_T^2$ and we therefore obtain the following V_T:

$$V_T = \frac{V_{T\infty}}{\left[\phi_w\left(1 + \phi_f\right)\right]^{1/2}} \tag{16}$$

Fig. 13 shows comparisons between the measured data and values

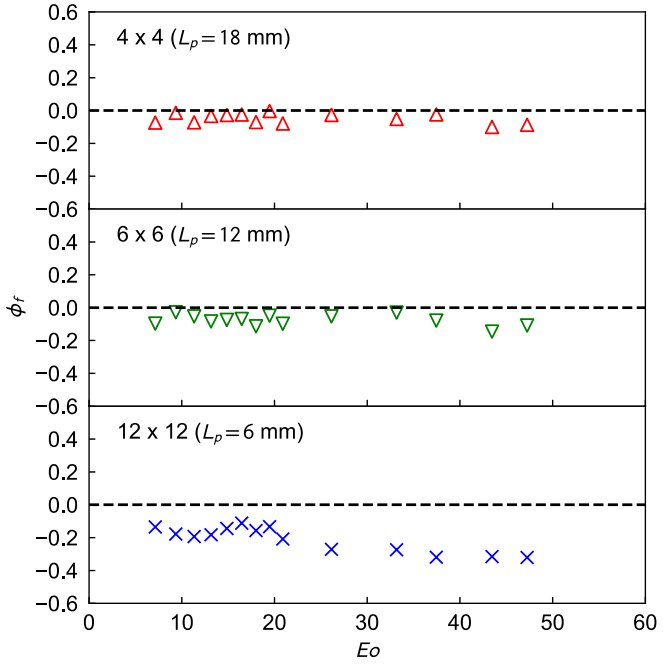

Fig. 11. Relation between ϕ_f and Eo for $Eo \geq 7.1$.

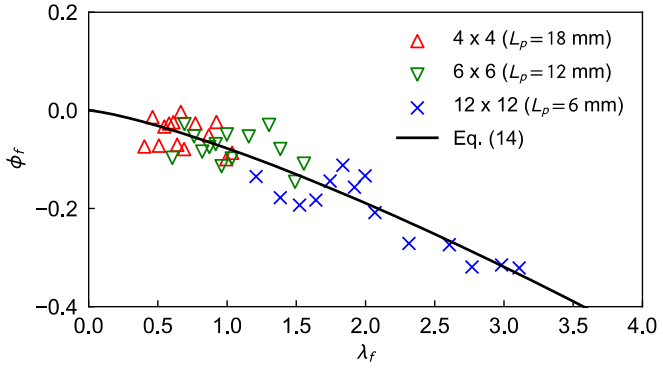

Fig. 12. Relation between ϕ_f and λ_f for $Eo > 7.1$.

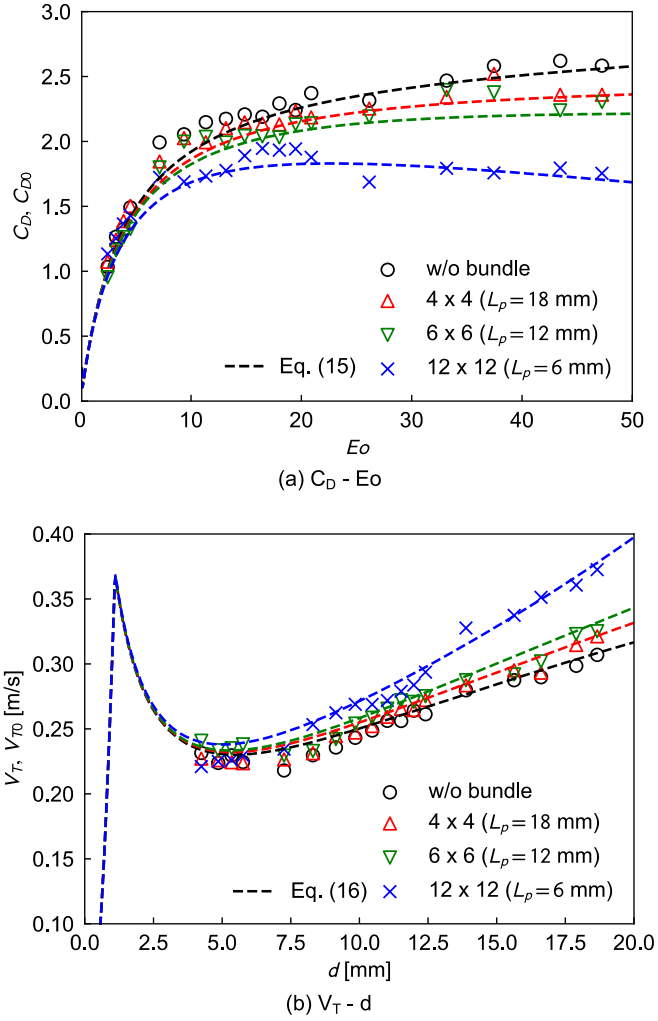

Fig. 13. Comparisons between measured and calculated drag coefficients and terminal velocities.

calculated by Eq. (15) or (16) with Eqs. (5), (11), and (14) on the C_D-Eo and V_T-d planes. The correlation gives good agreement with the measured data.

4. Conclusion

The shapes, terminal velocities, and horizontal motion of single bubbles rising through stagnant water in a vertically-aligned fiber bundle were measured. Three arrangements of fibers, 4 × 4, 6 × 6, and 12 × 12, the pitch L_p of which were 18, 12, and 6 mm, respectively, were tested in addition to the condition in the absence of fibers. The range of bubble diameter was from 4.2 to 18.7 mm, which implies that the bubbles were in the surface tension force and the inertial force dominant regime. The ranges of the bubble Reynolds number Re in the fiber bundle and the Eötvös number were $1050 \leq Re \leq 7800$ and $2.4 \leq Eo \leq 47$, respectively. Bubbles rising in the absence of fibers took either ellipsoidal, wobbling or cap shapes. The following conclusions were obtained:

(1) In the bubble diameter range that bubbles took wobbling or cap shapes in the absence of a fiber bundle, the terminal velocities of single bubbles increased with decreasing L_p, i.e., the drag coefficient for $Eo \geq 7.1$ decreased with decreasing L_p.
(2) The bubble aspect ratios increased for $Eo \geq 33$ indicating the shape change, once the velocity was expected to reduce with the increase in the aspect ratio. The observation from the top view showed that a bubble in the 12 × 12 fiber bundle without the central 2 × 2 fibers had a core region in the open space and several legs branched at fibers. This implied that large bubbles with a width much larger than L_p might take cross-like shapes in the 4 × 4, 6 × 6, and 12 × 12 bundles, which would contribute to the increase in the terminal velocity.
(3) The standard deviation σ* of the displacement of a bubble position σ* in the 12 × 12 bundle was remarkably suppressed in the wider range of d; in particular, σ* in both 6 × 6 and 12 × 12 bundles approached zero for λ_f (=d/L_p) ≥ 1.3.
(4) The multiplier ϕ_f for the effects of fiber bundles on the drag coefficient was well correlated in terms of λ_f.
(5) The terminal velocities of single bubbles in fiber bundles could be well predicted by combining the drag correlation in the absence of a fiber bundle and the fiber-effect multiplier ϕ_f.

CRediT authorship contribution statement

Ryo Kurimoto: Writing – original draft, Methodology, Investigation, Funding acquisition, Formal analysis, Conceptualization. **Roberta Fátima Neumeister:** Writing – original draft, Methodology, Investigation, Formal analysis. **Ryuya Komine:** Investigation, Formal analysis. **Gherhardt Ribatski:** Writing – review & editing, Investigation. **Kosuke Hayashi:** Writing – original draft, Investigation.

Declaration of competing interest

The authors declare that they have no known competing financial interests or personal relationships that could have appeared to influence the work reported in this paper.

Data availability

Data will be made available on request.

Acknowledgment

The authors would like to express their gratitude to Mr. Akiya Sumimoto for his assistance in experiments. This research was supported by JSPS KAKENHI (Grants No. 23K03660). The authors (Roberta F. Neumeister) acknowledge the support from FAPESP (Fundação de Amparo à Pesquisa do Estado de São Paulo) for the scholarships under the grant numbers 2022/03832-6 and 2023/09527-3.

Appendix A

Videos of bubbles rising through fiber bundle

.

Table A1
List of supplementary videos.

File name	Remarks
Supplementary video 1	$d = 5.8$ mm (6 × 6)
Supplementary video 2	$d = 10.5$ mm (6 × 6)
Supplementary video 3	$d = 18.7$ mm (6 × 6)
Supplementary video 4	$d = 5.8$ mm (12 × 12)
Supplementary video 5	$d = 10.5$ mm (12 × 12)
Supplementary video 6	$d = 18.7$ mm (12 × 12)
Supplementary video 7	Side & top views of $d = 25.8$ mm bubble (12 × 12 without 2 × 2 in center region)

Appendix B

Bubble shapes in 4 × 4 and 6 × 6 bundle.

Figs. B1 and B2 show bubble shapes in the 4 × 4 and 6 × 6 bundles, respectively. Two lines of fibers are assigned to the side of the bubble at $d =$ 18.7 mm in the 6 × 6 bundle, whereas only one line of fibers affects the bubble shape at the same d in the 4 × 4 bundle. Thus, the number of effective fibers on bubbles increases with decreasing L_p.

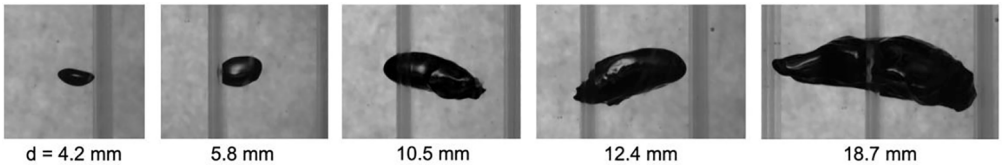

Fig. B1. Bubble shapes in 4 × 4 bundle

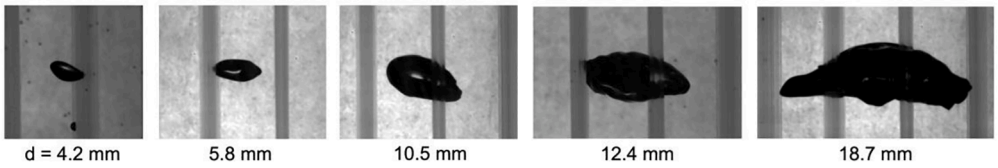

Fig. B2. Bubble shapes in 6 × 6 bundle

Appendix C

Measured V_T and V_{T0} in each bubble diameter.

Figure C1 shows the relations between the measured V_T and V_{T0} of bubbles and their averaged values at each d.

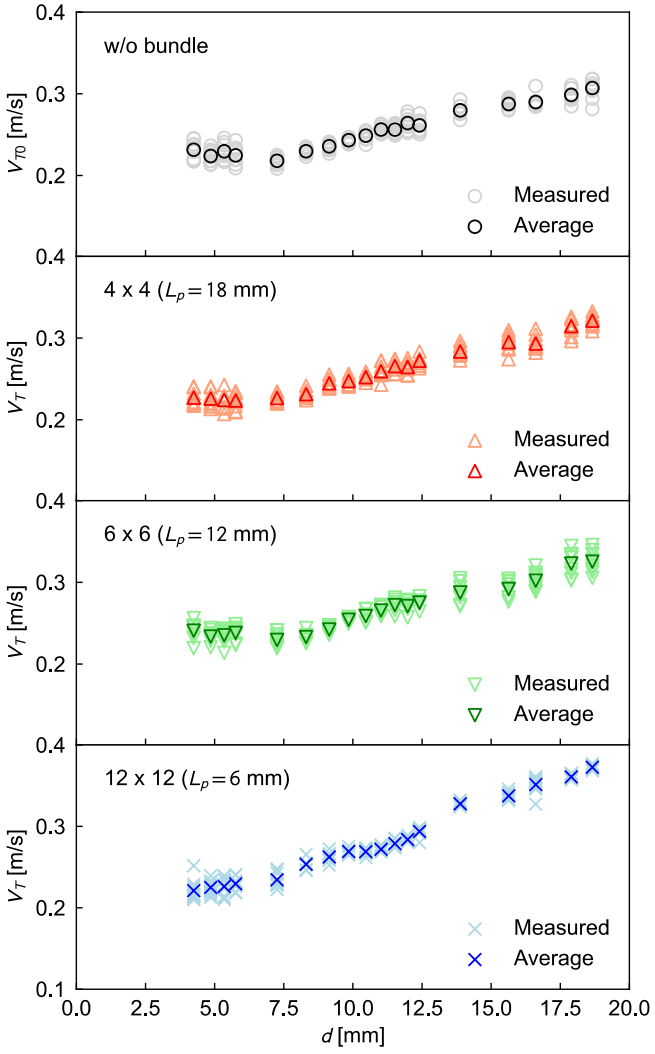

Fig. C1. Relation between measured terminal velocities and averaged values

Measured σ in each bubble diameter*

Figure C2shows the relations between the measured σ* and their averaged values at each *d*.

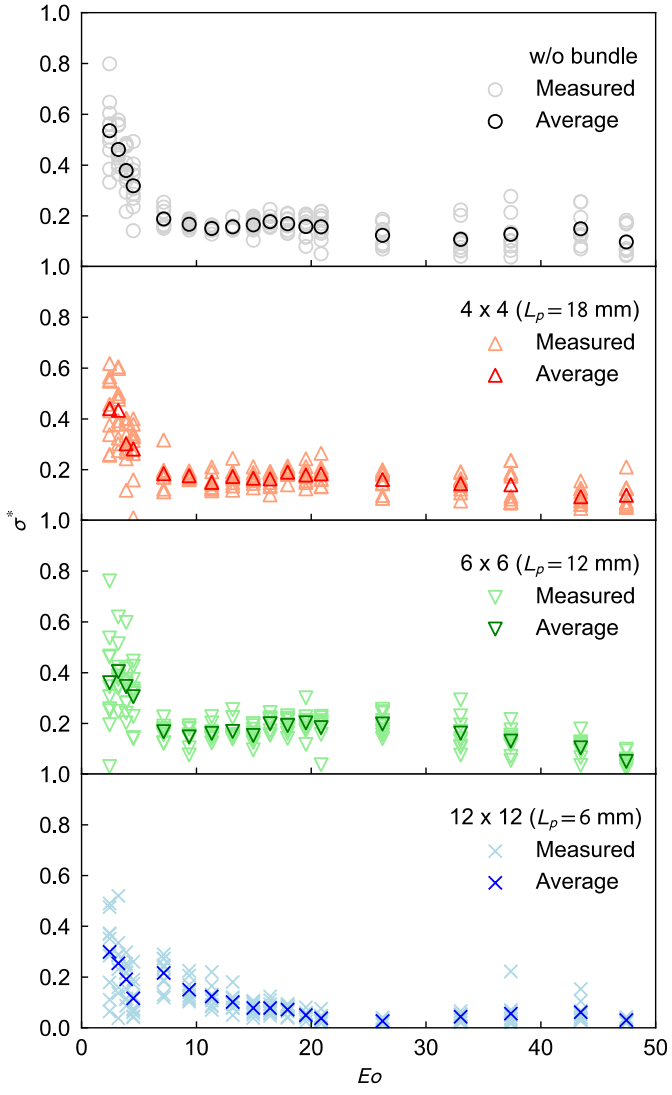

Fig. C2. Relation between measured σ* and averaged values

Appendix D

Velocity jump from $d = 12.4$ to 13.9 mm in 12×12 bundle.

As shown in Figs. 4, B1 and B2, the number of effective fibers on bubbles increases by the decrease in L_p, meaning that the increase in the number of effective fibers causes shape deformation of a bubble and the V_T increase. Figure D1 shows bubble images at $d = 12.4$ and 13.9 mm, where the former is the same image as the $d = 12.4$ mm bubble in Fig. 4(a). For the bubble at $d = 13.9$ mm, three lines of fibers are assigned to the side of the bubble in spite of only two lines of fibers for the bubble $d = 12.4$ mm. Thus, the number of effective fibers on bubble shapes increases between $d = 12.4$ and 13.9 mm, which contributes to the velocity jump from $d = 12.4$ to 13.9 mm in the 12×12 bundle.

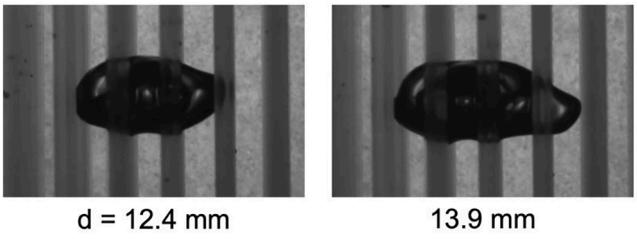

Fig. D1. Bubble images at $d = 12.4$ and 13.9 mm in 12×12 bundle

Appendix E. Supplementary data

Supplementary data to this article can be found online at https://doi.org/10.1016/j.ces.2024.120557.

References

Akhondi, E., Zamani, F., Tng, K.H., Leslie, G., Krantz, W.B., Fane, A.G., Chew, J.W., 2017. The performance and fouling control of submerged hollow fiber (HF) systems: a review. Appl. Sci. 7, 765.
Böhm, L., Drews, A., Prieske, H., Bérubé, P.R., Kraume, M., 2012. The importance of fluid dynamics for MBR fouling mitigation. Bioresour. Technol. 122, 50–61.
Cioncolini, A., Magnini, M., 2021. Shapes and rise velocities of single bubbles in a confined annular channel: experiments and numerical simulations. Fluids 6 (12), 437.
Clift, R., Grace, J.R., Weber, M.E., 1978. Bubbles, Drops, and Particles. Academic Press, New York, p. 1978.
Dumitrescu, D.T., 1943. Strömung an einer Luftblase im senkrechten Rohr. Z. Angew. Math. Mech. 23 (3), 139–149.
Hayashi, K., Kurimoto, R., Tomiyama, A., 2010. Dimensional analysis of terminal velocity of a Taylor bubble in a vertical pipe. Multiph. Sci. Technol. 22 (3), 197–210.
Inoue, M., Yusa, D., Nagaoka, H., 2016. Influence of hollow fiber membrane density on flow characteristic inside the membrane module in submerged MBRs. Journal of Japan Society of Civil Engineers, Ser. G (environmental Research) 72 (7). III_523-III_533 in Japanese.
Kurimoto, R., Hayashi, K., Tomiyama, A., 2013. Terminal velocities of clean and fully-contaminated drops in vertical pipes. Int. J. Multiphas. Flow 49, 8–23.
Kurimoto, R., Hayashi, K., Tomiyama, A., 2021. Removal of sludge attached to the wall of a planar vessel due to bubble motion. Multiph. Sci. Technol. 33 (3), 53–66.
Kurimoto, R., Takaya, S., Hayashi, K., Tomiyama, A., 2023. Bubbly flows in a column with submerged hollow fiber membranes. Chem. Eng. Res. Des. 200, 776–785.
Li, D., Neumann, A.W., 1992. Contact angles on hydrophobic solid surfaces and their interpretation. J. Colloid Interface Sci. 148 (1), 190–200.
Lin, J.W., Chang, H.C., 2011. Surface modification of SUS304 stainless steel by atmospheric pressure Ar/N_2/O_2 plasma. Nucl. Inst. Methods Phys. Res. B 269, 1801–1808.
Mori, T., Igarashi, R., Hayashi, K., Kurimoto, R., Tomiyama, A., 2024. Surface coverage ration of contaminated Taylor bubbles in a square microchannel. Chem. Eng. Res. Des. 204, 343–353.
Pan, R., Green, J., Maldarelli, C., 1998. Theory and experiment on the measurement of kinetic rate constants for surfactant exchange at an air/water interface. J. Colloid Interface Sci. 205, 213–230.
Radaei, E., Liu, X., Tng, K.H., Merendino, G., Trujillo, F.J., Bérubé, P.R., Leslie, G., 2019. Numerical and experimental investigation of pulse bubble aeration with high packing density hollow-fibre MBRs. Water Res. 160, 60–69.
Tang, K., Xie, J., Pan, U., Zou, X., Sun, F., Yu, Y., Xu, R., Jiang, W., Chen, C., 2022. The optimization and regulation of energy consumption for MBR process: A critical review. J. Environ. Chem. Eng. 10, 108406.
Tomiyama, A., 2004. Drag, lift and virtual mass forces acting on a single bubble, Proceedings of the 3rd International Symposium on Two-Phase Flow Modelling and Experimentation, CD-ROM, Pisa, Italy.
Tomiyama, A., Kataoka, I., Zun, I., Sakaguchi, T., 1998. Drag coefficients of single bubbles under normal and micro gravity conditions. JSME International Journal Seris B Fluids and Thermal Engineering 41 (2), 472–479.
Tomiyama, A., Celata, G.P., Hosokawa, S., Yoshida, S., 2002. Terminal velocity of single bubbles in surface tension force dominant regime. Int. J. Multiph. Flow 28, 1497–1519.
Tomiyama, A., Nakahara, Y., Adachi, Y., Hosokawa, S., 2003. Shapes and rising velocities of single bubbles rising through an inner subchannel. Jounrnal of Nuclear Science and Technology 40 (3), 136–142.
Venkateswararao, P., Semiat, R., Dukler, A.E., 1982. Flow pattern transition for gas-liquid flow in a vertical rod bundle. International Jornal of Multiphase Flow 8 (5), 509–524.
Wang, Z., Ma, J., Tang, C.Y., Kimura, K., Wang, Q., Hand, X., 2014. Membrane cleaning in membrane bioreactors: A review. J. Membr. Sci. 468, 276–307.
Wibisono, Y., Comelissen, E.R., Kemperman, A.J.B., van der Meer, Nijmeijer, K., 2014. Two-phase flow in membrane processes: A technology with a future. J. Membrane Sci. 453, 566–602.
Zhou, G., Prosperetti, A., 2021. Faster Taylor bubbles. J. Fluid Mech. 920, R2.